

WestminsterResearch

<http://www.westminster.ac.uk/westminsterresearch>

Graphene-based waveguide resonators for submillimeter-wave applications

Ilic, A.Z., Bukvic, B., Ilic, M.M. and Budimir, D.

This is an author's accepted manuscript of an article published in the Journal of Physics D: Applied Physics 49 (32), 325105 in 2016. The final definitive version is available online at: <https://dx.doi.org/10.1088/0022-3727/49/32/325105>

The WestminsterResearch online digital archive at the University of Westminster aims to make the research output of the University available to a wider audience. Copyright and Moral Rights remain with the authors and/or copyright owners.

Whilst further distribution of specific materials from within this archive is forbidden, you may freely distribute the URL of WestminsterResearch: (<http://westminsterresearch.wmin.ac.uk/>).

In case of abuse or copyright appearing without permission e-mail repository@westminster.ac.uk

Graphene based waveguide resonators for submillimeter-wave applications

Andjelija Ž Ilić¹, Branko Bukvić², Milan M Ilić^{2,3} and Djuradj Budimir⁴

¹ Institute of Physics, University of Belgrade, Pregrevica 118, 11080 Zemun-Belgrade, Serbia

² School of Electrical Engineering, University of Belgrade, Bulevar Kralja Aleksandra 73, 11120 Belgrade, Serbia

³ ECE Department, Colorado State University, Fort Collins, CO, USA

⁴ Wireless Communications Research Group, University of Westminster, London W1W 6UW, UK

E-mail: andjelijailic@ieee.org

Abstract. Utilization of graphene covered waveguide inserts to form tunable waveguide resonators is theoretically explained and rigorously investigated by means of full-wave numerical electromagnetic simulations. Instead of using graphene based switching elements, the concept we propose incorporates graphene sheets as parts of a resonator. Electrostatic tuning of the graphene surface conductivity leads to changes in the electromagnetic field boundary conditions at the resonator edges and surfaces, thus producing an effect similar to varying electrical length of a resonator. Presented outline of the theoretical background serves to give phenomenological insight into the resonator behavior, but it can also be used to develop customized software tools for design and optimization of graphene based resonators and filters. Due to the linear dependence of the imaginary part of the graphene surface impedance on frequency, the proposed concept was expected to become effective for frequencies above 100 GHz, which is confirmed by the numerical simulations. Frequency range from 100 GHz up to 1100 GHz, where the rectangular waveguides are used, is considered. Simple, all-graphene based resonators are analyzed first, to assess the achievable tunability and to check the performance throughout the considered frequency range. Graphene-metal combined waveguide resonators are proposed in order to preserve excellent quality factors typical for the type of waveguide discontinuities used. Dependence of resonator properties on key design parameters is studied in detail. Dependence of resonator properties throughout the frequency range of interest is studied using eight different waveguide sections appropriate for different frequency intervals. Proposed resonators are aimed at applications in the submillimeter-wave spectral region, serving as the compact tunable components for the design of bandpass filters and other devices.

1. Introduction

Millimeter and submillimeter wave region of electromagnetic (EM) spectrum is traditionally utilized in the astrophysics, remote sensing, defense and security, as well as in biomedical imaging applications [1–4]. Recently, there is an increased interest in utilization of these frequencies in a range of commercial applications, including broadband communications, motivated mainly by the availability of large bandwidths required for the multigigabit short-range wireless communications [5]. Consequently, there is a constant advance in the development of components and systems for millimeter and submillimeter wave frequencies [6–8]. Major limiting factor hindering broader exploitation of this spectral region for some time was the shortage of efficient low-cost power sources. With the recent increased research efforts in this direction, more efficient power sources are to be devised [4]. Another difficulty to be resolved is the choice of appropriate

materials for the design of devices and systems operating in this spectral region, i.e., at the boundary between microwaves and optics. Performance of PIN and varicap diodes, traditionally employed to obtain frequency reconfigurability and tunability, deteriorates with frequency. Micro electro-mechanical systems are used as an alternative; however, their switching speed is typically much lower and their power handling capability is low. Hence, there is a need to investigate alternative methods for attaining frequency tunability.

Graphene emerged, relatively recently, as a promising new material for photonics applications. In addition to its superior structural, mechanical and electrical properties, its electrically, magnetically and optically controllable conductivity makes it a good choice for the realization of tunable or reconfigurable components and devices. Electromagnetic field interaction with graphene at terahertz frequencies has been successfully investigated for a variety of applications including plasmonic antennas, wave modulators, and terahertz lasers [9–15]. Possible utilization of this controllable conductivity in the millimeter and submillimeter wave range has yet to be addressed more thoroughly. Method for microwave and millimeter wave characterization of graphene surface impedance, presented in [16], has been illustrated by material characterization at X and K_a bands. Reactive component of surface impedance at these frequencies is not large enough to produce significant frequency tunability, regardless of the wave attenuation in graphene. Frequency independent surface inductivity, as well as resistivity of graphene, lead to linear increase of reactive – versus the resistive impedance component ratio in the considered frequency range [17–18]. We show here that reasonable tunability can be achieved for frequencies above 100 GHz using the electrostatic tuning.

Rectangular waveguides and rectangular waveguide resonators are an attractive solution for millimeter and submillimeter applications requiring large power handling capability along with reasonably low losses. Additional good property of rectangular waveguides is a wide bandwidth of operation within the monomode regime. Dimensions and corresponding frequency ranges for the commercially available waveguide sections [19–20] operating at frequencies from about 100 GHz up to 1100 GHz are listed in table 1. A good five percent tunability has been achieved in our preliminary study [18] using graphene based resonators, where the focus was on the 300 GHz frequency, which is currently investigated as a good candidate for employment in the multigigabit short-range wireless communications. This work presents a significant extension of [18], where we have presented only a proof of concept that the chosen method of attaining frequency tunability could be successfully employed at higher frequencies. We here start with the development of theoretical expressions for electromagnetic fields in the vicinity of the proposed waveguide discontinuities, which for the first time give some physical insight into functioning principles of the suggested devices. Physics of graphene based resonators is further illustrated in the Results section, where an appropriately chosen example shows the impact on the electromagnetic boundary conditions and thus the field distribution of four distinct choices of the graphene stripe widths. The developed theoretical expressions are also applicable to other two-dimensional materials that could be developed in the future. In addition, they can be directly embedded in the specialized filter design software. Moreover, the necessity to perform certain trade-offs among the design parameters, indicated in [18], is now thoroughly investigated. In addition to the illustrative examples showing the resonance curves, detailed numerical electromagnetic analyses of dependence of tunability range, insertion loss, and loaded quality factor on the graphene stripe width are performed, systematically varying the width of the graphene stripe from nonexistent to completely covering the E-plane insert in steps of 2.5% of the insert length. Finally, the dependence of graphene based waveguide resonator properties on the frequency is investigated.

We here propose and investigate applications of graphene in waveguide resonators in the spectral region from 100 GHz to 1100 GHz. For the proposed applications we present the theoretical background and thorough numerical validations using rigorous full-wave computational simulations based on the method of moments (MoM), and the finite element method (FEM) algorithms. In analyses we consider standard rectangular waveguide sections as canonical examples for investigation of graphene efficiency in the considered frequency range, noting that graphene can be employed in the surface integrated waveguides and the hollow integrated waveguides as well. In particular, we study a single resonator, as a basic building block for millimeter and submillimeter wave filters.

An E -plane insert, considered in this study, is a waveguide discontinuity often employed in all-metal resonators and filters due to its simplicity and potential for accurate realization. Analytical expressions are initially derived to provide valuable insight into the underlying physical mechanisms of graphene based resonator operation. However, equivalent analytical models of E -plane inserts exhibit nonlinear frequency dependence around the desired central frequency of operation. Hence, accurate analysis of E -plane inserts requires numerical simulations or optimization algorithms [21]. Moreover, losses in graphene are higher than

in the purely metallic parts of the surrounding resonator structure, hence mandating full-wave numerical computations of wave propagation. Detailed investigation of the proposed structure is conducted using the full-wave computational electromagnetic analysis tools based on the MoM and FEM, namely utilizing, respectively, the state-of-the-art commercial software packages WIPL-D [22] and HFSS [23].

Table 1. Rectangular metallic waveguides: frequency bands and waveguide dimensions.

EIA Designation / Extended MIL[17]	IEEE Designation [16]	Frequency Range (GHz)	Cut-off (TE ₁₀) Frequency (GHz)	Aperture Width a (μm)	Aperture Height b (μm)
WR-10	WM-2540	75 – 110	59.01	2540.0	1270.0
WR-8	WM-2032	90 – 140	73.77	2032.0	1016.0
WR-6	WM-1651	110 – 170	90.79	1651.0	825.5
WR-5	WM-1295	140 – 220	115.75	1295.0	647.5
WR-4	WM-1092	170 – 260	137.27	1092.0	546.0
WR-3	WM-864	220 – 330	173.49	864.0	432.0
WR-2.8	WM-710	265 – 400	211.12	710.0	355.0
WR-2.2	WM-570	325 – 500	268.15	559.0	279.5
WR-1.9	WM-470	400 – 600	318.93	470.0	235.0
WR-1.5	WM-380	500 – 750	393.43	381.0	190.5
WR-1.2	WM-310	600 – 900	491.47	305.0	152.5
WR-1.0	WM-250	750 – 1100	590.15	254.0	127.0

2. Theoretical background

Standard rectangular waveguide section containing the resonator, which consists of two equally sized and symmetrically placed E -plane inserts, is shown in figure 1. The length of an E -plane insert, l_T , is represented as $l_T = l_M + l_G$ to include the case where only a part of an insert (of length l_G) is covered by graphene. Propagation of the transverse electric (TE) and transverse magnetic (TM) modes is supported above the cutoff frequency, given by $f_{c,mn} = \sqrt{((m/a)^2 + (n/b)^2) / 4\epsilon\mu}$, with integer m and n . These modes can be derived from a magnetic-type Hertzian potential and from an electric-type Hertzian potential, respectively [24]. Dominant mode of propagation is the TE₁₀ mode, since $a > b$ is usually considered. For standard waveguides $a = 2b$, so that $f_{c,20} = f_{c,01} = 2f_{c,10}$ and $f_{c,11} = \sqrt{5}f_{c,10}$, allowing for as large as possible single-mode bandwidth from $f_{c,10}$ to $2f_{c,10}$. Air filled waveguides are used in our analysis, with permittivity $\epsilon = \epsilon_0$ and permeability $\mu = \mu_0$.

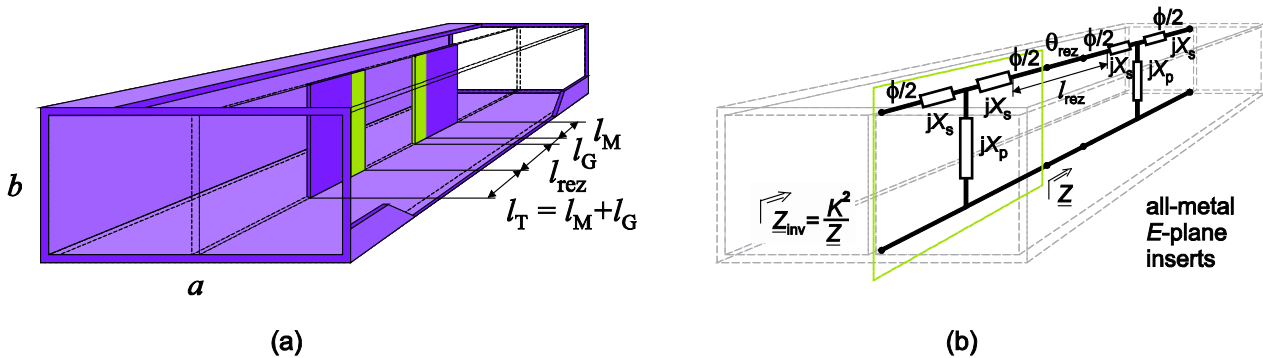


Figure 1. Waveguide resonator comprising two equal and symmetrically placed E -plane inserts: (a) the usual case of all-metal inductive inserts of the resonator, and (b) the normalized dominant mode equivalent circuit. When the resonator E -plane inserts consist of graphene layers, their surface impedance can be controlled via the bias voltage, influencing EM field distribution in the vicinity of waveguide discontinuities of total length l_T . The resulting effects are similar to the effects of varying the effective resonator length by changing the distance, l_{rez} , between the inserts. For the improved stop-band performance there should be the least difference in EM field distribution around the outer resonator edges, compared to the case of perfectly conducting inserts. This is addressed by applying graphene stripes, of length l_G , only along the inner edges of the resonator E -plane inserts, whereas the remaining part of each insert, of length l_M , is metallic.

Waveguide discontinuities lead to the excitation of higher order evanescent modes, which vanish at a distance from the discontinuity planes; however, changes are introduced in the reflection from and transmission through the considered section. Due to similarity of waveguide modal field solutions and wave propagation along a transmission line, formally identical systems of equations can be written for the modal field solutions and transmission line voltage and current relations. Namely, each mode can be represented as an equivalent transmission line, thus a circuit representation of waveguide discontinuities is possible. This is often utilized to facilitate analytical description of waveguide discontinuities.

2.1. All-metal E -plane resonators

Waveguide resonators and bandpass filters consisting of all-metal E -plane inserts were introduced as an answer to the need for an efficient, low cost, device, which can easily be mass-produced with desired accuracy [25]. Ever since, all-metal inserts remain appealing due to their small size and low losses.

Variational expression for the normalized admittance of an inductive insert is obtained according to [24], leading to the normalized dominant mode equivalent circuit of the discontinuity shown in figure 1(b). The equivalent symmetrical T-circuit of an E -plane insert can be symmetrically embedded in a length of a waveguide, incorporating the electrical length of $\phi/2$ on each port. With the convenient choice of ϕ , equivalent T-circuit acts as an impedance inverter, or K -inverter, in a very narrow frequency range. In an idealized impedance inverter, impedance seen at one port, Z , appears at the other port as $Z_{inv} = K^2/Z$. In the case of an E -plane insert, however, parameter K has nonlinear frequency dependence and can serve only as a first step approximation. Upon the calculation of equivalent circuit reactances X_s , X_p , normalized with respect to the waveguide characteristic impedance for the dominant mode, Z_C , the electrical length ϕ is chosen as

$$\phi = -\arctan(2X_p + X_s) - \arctan(X_s), \quad (1)$$

in order to approximate the equivalent circuit as a K -inverter defined by:

$$\tan(2\arctan K) = \frac{2X_p}{1 + 2X_p X_s + X_s^2}. \quad (2)$$

The normalized reactances, X_s and X_p , are functions of the length, l_T , of an E -plane insert. Frequency dependent parameters ϕ and K are in the first approximation calculated at some predefined ‘‘center’’ frequency, f_0 . The electrical length θ_{rez} , corresponding to the distance between the two inserts, l_{rez} , is then calculated taking into account the waveguide wavelength and subtracting the $\phi/2$ electrical lengths of the two impedance inverters, in this case equal. In accordance with the resonator and filter synthesis using the half-wave prototypes, the resulting electrical length must be equal to π at the frequency f_0 :

$$\theta_{rez} = l_{rez} \frac{\pi}{a} \sqrt{\epsilon_0 \mu_0 (2af_0)^2 - 1} - \phi = \pi. \quad (3)$$

Given X_s and X_p , the dimensions of a resonator can be approximately determined using (1) through (3).

To determine X_s and X_p , electromagnetic field in the vicinity of the insert of width g has to be represented as a sum of modal field solutions including the higher order modes, for the rectangular waveguide of width a and height b , on one side of the discontinuity plane, and for the two waveguides of width $(a-g)/2$ and height b , on the other side of the discontinuity plane. (Due to symmetry, only odd modes are required for the main waveguide.) Sufficient finite number of modes in an expansion has to be matched over the discontinuity plane, whereas the sum of field components at the metallic insert tends to zero (exactly equals zero for the perfect electric conductor (PEC)). For an accurate solution, computer aided calculations are required.

Alternatively, a commercial computer aided engineering (CAE) software tool can be used to determine the discontinuity scattering parameters, for different lengths of an insert in some predefined range of values. Equivalent T-circuit normalized reactances are obtained from S -parameters as:

$$jX_s = \frac{1 + S_{11} - S_{21}}{1 - S_{11} + S_{21}}, \quad jX_p = \frac{2S_{21}}{(1 - S_{11})^2 - S_{21}^2}. \quad (4)$$

2.2. Dielectric slab with and without conductive layer

If a metallic E -plane insert, or any part of it, is to be replaced by graphene, a dielectric holder is needed as a support. Phase shifts of the guided wave, introduced by the dielectric slab, should be accounted for in the

resonator design. In our case, dielectric slab of finite length, l_T , is placed asymmetrically as shown in figure 2, so that the very thin layer of metallization or a graphene layer runs along the midline of the waveguide. An excellent example of analysis of asymmetrically placed dielectric slab, without the conductive layer, is given in [26] including the complete final expressions needed to numerically calculate the scattering matrix. Very limited outline of the major derivation steps pertinent to the special case in figure 2 will be given next.

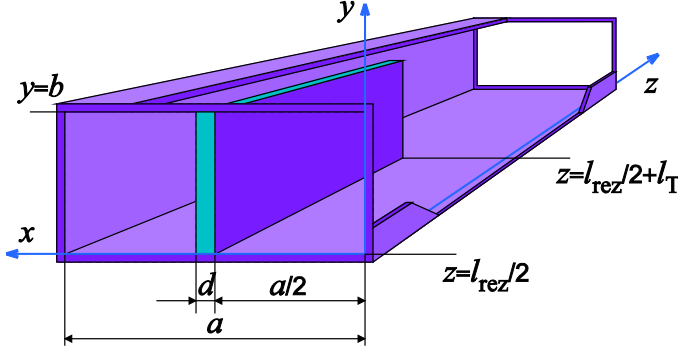


Figure 2. Waveguide discontinuity comprising a dielectric slab of finite length, l_T , and thickness, d , and a layer of metallization or graphene of negligible thickness covering the dielectric slab side along the midline of the waveguide. Coordinate system shown is used in analytical expressions throughout the paper.

Since the discontinuity is uniform along the y -axis, higher order modes excited at the junction are the TE_{m0} modes. The appropriate x -component of the Hertzian vector potential for the considered case is

$$Q_x = \begin{cases} \sum_{m=1}^{\infty} A_m^I \sin\left(\frac{m\pi}{a}x\right) e^{-jk_{zm}^I z}, & 0 \leq z \leq \frac{l_{rez}}{2} \text{ or } z \geq \frac{l_{rez}}{2} + l_T, 0 \leq x \leq a, \text{ (region I)} \\ \sum_{m=1}^{\infty} \left(A_m^{II} \cos(k_{xm}^D x) + B_m^{II} \sin(k_{xm}^D x) \right) e^{-jk_{zm}^D z}, & \frac{l_{rez}}{2} \leq z \leq \frac{l_{rez}}{2} + l_T, \frac{a}{2} \leq x \leq \frac{a}{2} + d, \text{ (region II)} \\ \sum_{m=1}^{\infty} A_m^{III} \left(-\tan(k_{xm}^A a) \cos(k_{xm}^A x) + \sin(k_{xm}^A x) \right) e^{-jk_{zm}^A z}, & \frac{l_{rez}}{2} \leq z \leq \frac{l_{rez}}{2} + l_T, \frac{a}{2} + d \leq x \leq a, \text{ (region III)} \\ \sum_{m=1}^{\infty} A_m^{IV} \sin(k_{xm}^A x) e^{-jk_{zm}^A z}, & \frac{l_{rez}}{2} \leq z \leq \frac{l_{rez}}{2} + l_T, 0 \leq x \leq \frac{a}{2}, \text{ (region IV)} \end{cases} \quad (5)$$

Three components of the electromagnetic field vanish, namely: $E_x = 0$, $H_y = 0$, $E_z = 0$. The nonzero components of the electromagnetic field are calculated using:

$$E_y = -j\omega\mu_0 \frac{\partial Q_x}{\partial z}, \quad H_x = \omega^2 \mu_0 \epsilon_0 \epsilon_r Q_x + \frac{\partial^2 Q_x}{\partial x^2}, \quad H_z = \frac{\partial^2 Q_x}{\partial x \partial z}. \quad (6)$$

In the above, $\omega = 2\pi f$ is the angular frequency and ϵ_r is the relative permittivity, considered equal to unity everywhere except in the region II, which is defined by (5) for the coordinate system given in figure 2. Equality of the tangential field components, E_y and H_z , at the regions interfaces at $x = a/2$ and $x = a/2 + d$ yields a system of linear equations. For a non-trivial solution, the system's determinant has to vanish, leading to a transcendental equation for the transverse mode propagation constants in air, k_{xm}^A , and in dielectric, k_{xm}^D :

$$\tan(k_{xm}^D d) + \frac{k_{xm}^D}{k_{xm}^A} \left(\tan(k_{xm}^A \frac{a}{2}) + \tan(k_{xm}^A (\frac{a}{2} - d)) \right) - \left(\frac{k_{xm}^D}{k_{xm}^A} \right)^2 \tan(k_{xm}^D d) \tan(k_{xm}^A \frac{a}{2}) \tan(k_{xm}^A (\frac{a}{2} - d)) = 0. \quad (7)$$

Both k_{xm}^A and k_{xm}^D are expressed in terms of the longitudinal propagation factor k_{zm} , that is equal for regions II, III, and IV, defined by (5) and figure 2. Equation (7) is numerically solved for k_{zm} , further determining

$$k_{xm}^A{}^2 = k_0^2 - k_{zm}^2, \quad k_{xm}^D{}^2 = \epsilon_r k_0^2 - k_{zm}^2, \quad k_0^2 = \omega^2 \mu_0 \epsilon_0. \quad (8)$$

With respect to the longitudinal propagation factors of the main waveguide, k_{zm}^I , obtained from $k_{zm}^I{}^2 = k_0^2 - (\frac{m\pi}{a})^2$, amplitudes of the modal propagation constants, k_{zm} , are larger, implying shorter modal wavelengths. Considering the TE_{10} mode, the only one that can actually propagate in the main waveguide, the discontinuity section can be viewed as if it is filled with material of an equivalent dielectric constant ϵ_{re} , given by $\epsilon_{re} = k_0^{-2} (k_{z1}^2 + (\pi/a)^2)$, reducing the phase velocity by a factor of $\sqrt{\epsilon_{re}}$. The phase shift introduced by the dielectric slab is approximately equal to

$$\Delta\theta_D = l_T \left(|k_{z1}| - \sqrt{k_0^2 - \left(\frac{\pi}{a}\right)^2} \right). \quad (9)$$

If the dielectric slab side at $x=a/2$ were covered with a negligibly thick PEC sheet ($g \rightarrow 0$), the boundary conditions would dictate the vanishing of the tangential field components, E_y and H_z , at both sides of the PEC sheet. This simplifies the field equations derived from the following x -component of the Hertzian potential:

$$Q_x = \begin{cases} \sum_{m=1}^{\infty} A_m^I \sin\left(\frac{m\pi}{a}x\right) e^{-jk_{zm}^I z}, & 0 \leq z \leq \frac{l_{rez}}{2} \text{ or } z \geq \frac{l_{rez}}{2} + l_T, 0 \leq x \leq a, \text{ (region I)} \\ \sum_{m=1}^{\infty} A_m^{II} \left(-\tan\left(k_{xm}^D \frac{a}{2}\right) \cos(k_{xm}^D x) + \sin(k_{xm}^D x) \right) e^{-jk_{zm}^I z}, & \frac{l_{rez}}{2} \leq z \leq \frac{l_{rez}}{2} + l_T, \frac{a}{2} \leq x \leq \frac{a}{2} + d, \text{ (region II)} \\ \sum_{m=1}^{\infty} A_m^{III} \left(-\tan(k_{xm}^A a) \cos(k_{xm}^A x) + \sin(k_{xm}^A x) \right) e^{-jk_{zm}^I z}, & \frac{l_{rez}}{2} \leq z \leq \frac{l_{rez}}{2} + l_T, \frac{a}{2} + d \leq x \leq a, \text{ (region III)} \\ \sum_{m=1}^{\infty} A_m^{IV} \sin\left(\frac{2m\pi}{a}x\right) e^{-jk_{zm}^{IV} z}, & \frac{l_{rez}}{2} \leq z \leq \frac{l_{rez}}{2} + l_T, 0 \leq x \leq \frac{a}{2}, \text{ (region IV)} \end{cases}. \quad (10)$$

In the above, $k_{zm}^{I2} = k_0^2 - \left(\frac{m\pi}{a}\right)^2$ and $k_{zm}^{IV2} = k_0^2 - \left(\frac{2m\pi}{a}\right)^2$, whereas $k_{zm}^{II} = k_{zm}^{III} = k_{zm}^I$ is obtained from

$$\tan(k_{xm}^D d) + \frac{k_{xm}^D}{k_{xm}^A} \tan\left(k_{xm}^A \left(\frac{a}{2} - d\right)\right) = 0, \quad (11)$$

using dependencies given in (8). For a metal of finite conductivity σ_m , and permeability μ_0 , surface impedance of the thin metal sheet can be calculated as $Z_S = (1+j)\sqrt{\pi f \mu_0 / \sigma_m}$. It corresponds to the ratio of the total tangential electric field component and total tangential magnetic field component at any point on a surface, i.e., $Z_S = E_y / H_z$ for a thin metallic sheet located at $x=a/2$. The attenuation is small and electromagnetic field distribution is almost identical to the PEC case.

2.3. Influence of the graphene surface conductivity

Surface conductivity of graphene, in the considered range of frequencies, stems solely from the intraband contributions. It is given by [17,27]

$$\sigma(\omega, \mu_c, \Gamma, T) = \frac{-jq_e^2 k_B T}{\pi \hbar^2 (\omega - j2\Gamma)} \left(\frac{\mu_c}{k_B T} + 2 \ln\left(e^{-\frac{\mu_c}{k_B T}} + 1\right) \right), \quad (12)$$

where ω is the angular frequency, μ_c is the chemical potential of graphene, Γ represents the carrier scattering rate, T is the temperature, and k_B the Boltzmann constant. The chemical potential, μ_c , $k_B T$ product, as well as the scattering rate, Γ , are expressed in electronvolts, although Γ in s^{-1} is used in (12). Elementary charge and the reduced Planck constant are denoted as q_e and \hbar , respectively. Room temperature, $T = 300$ K, is assumed throughout the paper. The above equation is accurate at room temperature, in the millimeter and submillimeter wave frequency range where spatial-dispersion effects are negligible, provided that there is no magnetic field bias. The chemical potential, μ_c , depends on the level of chemical doping; however, it is also tunable using the relation between the chemical potential and the electrostatic bias field, E_{bias} [27]:

$$\frac{\varepsilon_0 \pi \hbar^2 v_F^2}{q_e} E_{bias} = \int_0^{+\infty} \mathfrak{g} \left[(1 + e^{(\mathfrak{g} - \mu_c)/k_B T})^{-1} - (1 + e^{(\mathfrak{g} + \mu_c)/k_B T})^{-1} \right] d\mathfrak{g}. \quad (13)$$

Electrostatic bias field, perpendicular to the graphene surface, is created by applying the bias voltage across the capacitor formed by the graphene layer and the gating electrode, separated by a thin dielectric layer. A metallic gating electrode in proximity to the graphene layer would affect the electromagnetic wave propagation; a metallic layer parallel to the graphene surface would itself present an E -plane insert, masking the effects of the tunable conductivity of graphene. Therefore, another graphene layer has to play the role of the gate electrode. Utilization of such all-graphene gating and the graphene stacks, structures composed of two or more graphene layers separated by electrically thin dielectrics, has been theoretically investigated and experimentally verified [9,12,28–30]. Alumina, Al_2O_3 , is often employed as the dielectric layer in-between

the graphene sheets. We will assume a 100 nm thick Al_2O_3 layer, which is thick enough to neglect the quantum capacitance of graphene, but still sufficiently thin to allow for the low bias voltages of the graphene-based top gate. From the point of view of electromagnetic wave propagation, the described graphene stack is electrically very thin and the boundary conditions can be assumed constant throughout the graphene stack. Likewise, very small slits needed to connect the outer voltage generator to the two graphene layers are not deemed influential on the EM field distribution along the resonator edges nor the further EM wave propagation. Without the loss of generality, we will perform numerical electromagnetic modeling of the proposed structures, replacing the graphene stacks with single layers of negligible thickness exhibiting tunable surface conductivity. All of the results will be given for several chemical potentials in the range of interest, rather than for the corresponding bias voltages, thus allowing for easier interpretation of results, once actual biasing conditions and the equivalent total stack conductivity are determined [29]. The Fermi velocity in graphene is $v_F \approx 10^6 \frac{\text{m}}{\text{s}}$ and the chemical potential is easily tuned in the range $[-1 \text{ eV}, 1 \text{ eV}]$. Graphene surface impedance, $Z_g = R_g + j\omega L_g$, is obtained directly, with the surface resistance and surface inductance given by

$$R_g = 2\Gamma \frac{q_e}{\hbar} L_g, \quad L_g = \frac{\pi \hbar^2}{q_e^3 k_B T \left(\frac{\mu_c}{k_B T} + 2 \ln(e^{-\mu_c / (k_B T)} + 1) \right)}. \quad (14)$$

The Boltzmann constant $k_B = 8.6173325 \times 10^{-5} \text{ eV/K}$ and the reduced Planck constant $\hbar = 1.054571726 \times 10^{-34} \text{ Js}$ are used, whereas μ_c is varied in the range $[-1 \text{ eV}, 1 \text{ eV}]$.

If in the dielectric slab configuration shown in figure 2, the slab side located at $x = a/2$ is covered with a graphene layer, electromagnetic field at this boundary surface will be significantly reduced compared with the pure dielectric slab. This effect is brought by the graphene conductivity, leading to the resonating effect when there are two conducting surfaces as in figure 1. Still, EM field at $x = a/2$ will be far from zero, due to the finite, much larger than in the metallic case, real part of the surface impedance, $R_g \gg \sqrt{\pi f \mu_0 / \sigma_m}$, in the frequency range of interest. The real part of the surface impedance induces attenuation of the guided wave, whereas the imaginary, reactive component of the surface impedance is responsible for the resonant frequency shift. This is illustrated in figure 3, for the standard WR-3 waveguide section. High quality, low resistivity graphene, should be used to minimize losses.

The appropriate x -component of the Hertzian vector potential is again given by (5). There is no need to introduce the new region at $x = a/2$, since the total tangential electric fields, E_y , can be considered constant at both sides and throughout the graphene layers belonging to the electrically thin conductive sheet. At the interface of regions II and III, where there are no free charges or currents, E_y , as well as H_z , have to be continuous over the interface. In order to satisfy the electric field boundary conditions at the graphene surface at $x = a/2$, and at $x = a/2 + d$ boundary, we have to enforce the equality of the longitudinal propagation factor, k_{zm} , for the regions II, III, and IV. Resulting from the total E_y , the surface current density of the graphene sheet equals $\mathbf{J}_S = \sigma E_y \hat{y} = Z_g^{-1} E_y \hat{y}$. It is also related to the tangential magnetic fields at $x = a/2$, through $\mathbf{J}_S = \hat{n} \times (H_z^{\text{IV}} - H_z^{\text{II}}) \hat{z}$, where $\hat{n} \equiv -\hat{x}$ represents the region IV surface normal. We thus develop the field components, E_y and H_z , in the regions II, III, and IV using (6). Appropriate boundary conditions lead to the following system of equations:

$$\begin{bmatrix} \cos(k_{xm}^{\text{D}} \frac{a}{2} + d) & \sin(k_{xm}^{\text{D}} \frac{a}{2} + d) & \frac{\sin(k_{xm}^{\text{A}} (\frac{a}{2} - d))}{\cos(k_{xm}^{\text{A}} a)} & 0 \\ k_{xm}^{\text{D}} \sin(k_{xm}^{\text{D}} \frac{a}{2} + d) & -k_{xm}^{\text{D}} \cos(k_{xm}^{\text{D}} \frac{a}{2} + d) & \frac{k_{xm}^{\text{A}} \cos(k_{xm}^{\text{A}} (\frac{a}{2} - d))}{\cos(k_{xm}^{\text{A}} a)} & 0 \\ \cos(k_{xm}^{\text{D}} \frac{a}{2}) & \sin(k_{xm}^{\text{D}} \frac{a}{2}) & 0 & -\sin(k_{xm}^{\text{A}} \frac{a}{2}) \\ k_{xm}^{\text{D}} \sin(k_{xm}^{\text{D}} \frac{a}{2}) & -k_{xm}^{\text{D}} \cos(k_{xm}^{\text{D}} \frac{a}{2}) & 0 & \frac{j\omega\mu_0}{Z_g} \sin(k_{xm}^{\text{A}} \frac{a}{2}) + k_{xm}^{\text{A}} \cos(k_{xm}^{\text{A}} \frac{a}{2}) \end{bmatrix} \begin{bmatrix} A_m^{\text{II}} \\ B_m^{\text{II}} \\ A_m^{\text{III}} \\ A_m^{\text{IV}} \end{bmatrix} = \begin{bmatrix} 0 \\ 0 \\ 0 \\ 0 \end{bmatrix}. \quad (15)$$

For a non-trivial solution, the system's determinant has to vanish, yielding

$$\xi_g \cdot \tan(k_{xm}^D d) + \frac{k_{xm}^D}{k_{xm}^A} \left(\tan(k_{xm}^A \frac{a}{2}) + \xi_g \cdot \tan(k_{xm}^A (\frac{a}{2} - d)) \right) - \left(\frac{k_{xm}^D}{k_{xm}^A} \right)^2 \tan(k_{xm}^D d) \tan(k_{xm}^A \frac{a}{2}) \tan(k_{xm}^A (\frac{a}{2} - d)) = 0, \quad (16a)$$

$$\xi_g = 1 + \frac{j\omega\mu_0}{Z_g k_{xm}^A} \tan(k_{xm}^A \frac{a}{2}), \quad \xi_g = 1 + \frac{\omega^2 L_g \mu_0 a + j\omega R_g \mu_0 a}{2(R_g^2 + \omega^2 L_g^2)} \frac{\tan(k_{xm}^A \frac{a}{2})}{k_{xm}^A a/2}. \quad (16b)$$

In the limit $Z_g \rightarrow 0$, we have to multiply the equation (16a) with Z_g . The only remaining non-zero terms result in

$\left(\sin k_{xm}^{IV} \frac{a}{2} \right) \left(\tan(k_{xm}^D d) + \frac{k_{xm}^D}{k_{xm}^A} \tan(k_{xm}^A (\frac{a}{2} - d)) \right) = 0$, leading to the equations (10) and (11). In the limit $Z_g \rightarrow \infty$, we obtain $\xi_g = 1$, and (16a) reduces to the equation (7), describing the purely dielectric slab.

In between the two limits, Z_g modifies EM fields significantly, dependent on intrinsic material properties, frequency, and the applied bias field. With a change in Z_g , evanescent higher order modes of the coated surface at $x = a/2$ decrease in magnitude with varying longitudinal propagation factors. As a result, elements of the equivalent T-circuit in figure 1(b) become tunable. Changes in the equivalent circuit elements are reflected in the varying appropriate electrical length ϕ needed to obtain the function of the K -inverter element, further affecting the total electrical length of a resonator, θ_{rez} . In short, the tunable graphene surface impedance can be considered as a tunable effective length of the E -plane inserts, changing the length of a resonator, and thus leading to the change in its resonant frequency. As the modifications of resonator length are desired, there is no benefit in changing the overall length of the section comprising the two E -plane inserts, i.e., the all-metal inserts exhibit the best stop band performance. This led us to the proposal of the graphene-metal combined waveguide resonators, where an inner side of each E -plane insert adjacent to the resonator, l_{rez} , is coated with graphene, whereas the rest of the inserts is purely metallic. With the aid of numerical simulations, different configurations will be analyzed and compared in the following sections.

2.4. Full-wave electromagnetic analysis

The numerical simulations assume quartz as a support for graphene layers and a thin film metallization. This choice has been motivated by two reasons. Firstly, fused silica quartz is an excellent substrate for the millimeter and submillimeter wave applications due to the relatively low dielectric constant and a small loss tangent. Secondly, quartz is a substrate material highly compatible with graphene. In addition to very usual wet-etching techniques for the transfer of graphene films grown on another substrate [31], there are also many recent techniques for direct generation of graphene on quartz, e.g., laser-based direct synthesis [32]. Reasonable adhesion of metallic thin films, copper (Cu) and gold (Au), on quartz, requires somewhat more complicated deposition techniques. Thin film metallization on quartz is usually comprised of two layers, the first one being a strongly oxidized metal such as chromium or titanium [33,34]. The quartz dielectric constant and loss tangent equal $\epsilon_r = 3.78$ and $\tan \delta = 0.000228$, respectively. Quartz substrate thickness for the WR-3 waveguide is chosen as the commercially available 50 μm . For consistency, the ratio of quartz support thickness and the waveguide broad wall is kept equal to $d/a = 1/16$ for all considered waveguide sections, given in table 1. Close to 1 THz, a different material might be a better choice. In that case, phase shift and loss could differ with the same qualitative behavior of resonators.

In the analyses of the graphene-metal combined waveguide resonators we assume a thin film metallization of Cu for the WR-6, WR-4 and WR-3 waveguide sections, and a thin film metallization of Au in all other cases. The skin effect has been modeled accordingly, taking the DC conductivities of Cu and Au, $\sigma_{Cu} = 58.0 \text{ MS/m}$ and $\sigma_{Au} = 41.0 \text{ MS/m}$, respectively. It has been shown previously, that the losses in graphene stripe were dominant in comparison with metallization as well as dielectric loss [18]; therefore, the effects of the metallization surface roughness were not considered here.

As mentioned above, the surface conductivity of graphene at room temperature, for a given frequency, depends on the chemical potential of graphene, μ_c , and the carrier scattering rate, Γ . The chemical potential, related to the level of chemical doping and the applied electrostatic bias field, is easily tuned in the range $[-1 \text{ eV}, 1 \text{ eV}]$, with the $\pm[0.2 \text{ eV}, 1.0 \text{ eV}]$ interval of interest in this study. This choice of working interval corresponds to the concentration of charge carriers that is already somewhat increased, either by the chemical doping, or by the initially applied bias voltage. Further biasing allows for the precise control of the chemical

potential, and thus the attained low resistivity, as the chemical potential variation with bias voltage in this interval is less steep than at zero chemical potential. Additionally, the relation between the chemical potential and the electrostatic bias field is more linear, as shown in figure 3 in [27]. The phenomenological scattering rate, Γ , is related to the relaxation time of charge carriers, $\tau = (2\Gamma)^{-1}$, which can differ significantly in the cases of intrinsic and doped graphene [35]. Carrier relaxation time at subterahertz frequencies can be identified with the DC relaxation time, $\tau \approx \tau_{DC} = \mu \hbar \sqrt{n_c} \pi / (q_e v_F)$, which arises mainly from impurities [36]. DC relaxation time is directly proportional to the charge carrier mobility, μ , and the square root of the carrier concentration, n_c . Experimental investigation of high-purity graphene, found in nature on the surface of bulk graphite, sets the low temperature scattering time limit at $\tau \approx 20$ ps [35]. High mobility of charge carriers has also been obtained in case of the suspended graphene [37,38], up to $\mu = 200\,000$ cm²/(Vs) at low temperatures and $\mu = 120\,000$ cm²/(Vs) near room temperature. Influence of substrate type and quality on carrier mobility can be significant. In a study utilizing the Monte Carlo method to investigate the substrate influence on the carrier mobility for three different substrates [39], high charge carrier mobility was obtained only for the hexagonal boron nitride (h-BN) substrate ($\mu \approx 170\,000$ cm²/(Vs)). That finding is in accordance with the experimental results [40]. High carrier mobility has been observed for the multiple-graphene-layer (MGL) structures grown epitaxially on SiC, as well [14,41–44]. Growth on the Si-face of SiC results in a lower mobility few-layer graphene, whereas growth on the C-face results in a high mobility multilayer graphene ($\mu \approx 200\,000$ cm²/(Vs)). The number and mobility of graphene layers can thus be controlled by controlling the crystal orientation of the SiC. Once fabricated, such MGL structures can be transferred to a different substrate [44]. The real part of the intraband graphene conductivity always contributes as a loss. Since introducing large losses is highly undesirable in the waveguiding applications, high-quality low-loss graphene should be used. Therefore, the moderately long relaxation time, $\tau = 3$ ps, is considered in the numerical examples. The impact of the carrier relaxation time on tunability and insertion loss of the proposed waveguide resonators is illustrated in figure 4.

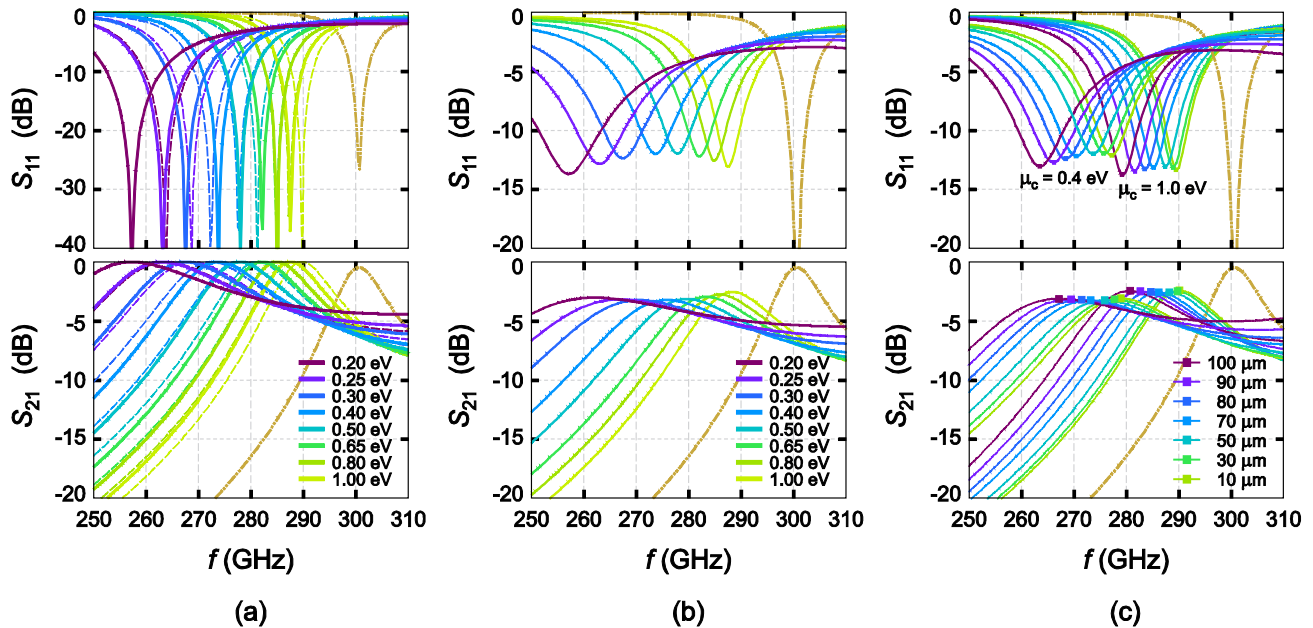


Figure 3. Effects on the resonator parameters of (a) the graphene surface inductance only, with R_g set to zero, (b) the realistic graphene surface impedance, and (c) the quartz support thickness. Standard WR-3 waveguide section with $l_{rez} = 360$ μ m, and $l_T = 280$ μ m completely covered by the graphene layers, was analyzed. Scattering parameters for the all-metal case, with the $f_{rez}^M = 300.75$ GHz, are presented by the dash-dot-dot line in all graphs. In part (a), the dashed lines correspond to the two-dimensional graphene sheet without a dielectric support revealing the tunability effect due to the graphene only, whereas the solid lines show the combined resonant frequency shifts and tunability due to the graphene-on-quartz. Additional phase shifts introduced by the dielectric slab are functions of the graphene surface inductance, resulting in a broader tunability range when the dielectric support is used. Different line colors (shades) in parts (a) and (b) correspond to the graphene chemical potential values given in the legend. Scattering parameters accounting for the realistic loss in graphene-on-quartz resonators are shown in part (b). Results of an investigation into the effect of the quartz thickness on S -parameters are shown in part (c), through a comparison of S -parameters for two values of graphene chemical potential: 0.4 eV and 1.0 eV. Larger thickness yields a slightly broader tunability range, however at the expense of a larger shift between the reflected and the transmitted wave and somewhat worse quality factor (line colors/shades are explained in the legend). Therefore, the dielectric support should remain thin.

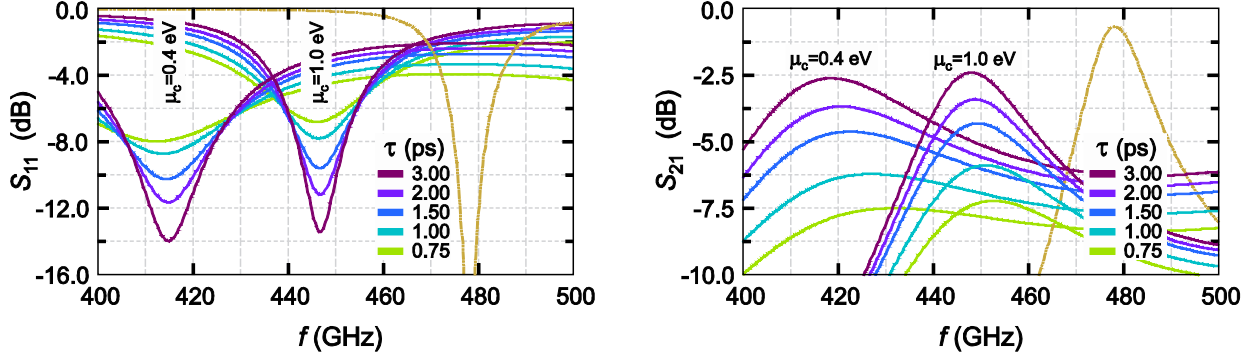


Figure 4. Dependence of the resonator S -parameters on the relaxation time of charge carriers, τ . Results are presented for the standard WR-2.2 waveguide section with $l_{\text{rez}} = l_{\text{T}} = 210 \mu\text{m}$, with l_{T} completely covered by the graphene layers (line colors/shades are explained in the legend). The S -parameters corresponding to the all-metal resonator are given for comparison by the dash-dot-dot line ($f_{\text{rez}}^{\text{M}} \cong 478 \text{ GHz}$). Results are shown for two values of the graphene chemical potential: 0.4 eV and 1.0 eV. There is no impact of the carrier relaxation time on tunability range. However, the observed increase in the insertion loss makes the concept impractical for low quality graphene layers.

The tunability effect achieved by the utilization of the adjustable graphene surface impedance in resonators comprised of E -plane inserts stems from the adjustment of the boundary conditions, as described by equations (16a) and (16b). Numerical analysis of a resonator using the WR-3 waveguide section is performed first, to qualitatively illustrate the effects on the resonator parameters of the real and imaginary parts of the surface impedance as well as the dielectric support thickness. As listed in table 2, the resonator length and the E -plane insert length were chosen as $l_{\text{rez}} = 360 \mu\text{m}$ and $l_{\text{T}} = 280 \mu\text{m}$, respectively. The results are shown in figure 3. For this first resonator, all-graphene E -plane inserts were considered, i.e. the quartz support of the total length l_{T} was assumed to be covered completely by the graphene. Simulations confirm the dependence of the obtained tunability range on the graphene surface inductance, both with $R_{\text{g}} = 0$ and $R_{\text{g}} \neq 0$. The real part of the graphene surface impedance contributes as a loss, on the order of 3 dB for the considered case. Lower mobility graphene sheets have the same dependence of the graphene surface inductance on the chemical potential; therefore, the tunability range remains the same, regardless of the carrier relaxation time. Insertion loss, on the other hand, increases, which suggests that the low quality graphene is not appropriate for the considered resonator type. This has been illustrated by the results shown in figure 4, corresponding to several values of the carrier relaxation time, τ , and the WR-2.2 waveguide section with $l_{\text{rez}} = l_{\text{T}} = 210 \mu\text{m}$. Slightly broader tunability range with the increase in dielectric slab thickness, as seen from the figure 3, does not compensate for the deteriorated quality factor and the larger frequency mismatch between the reflected and the transmitted wave; therefore, it should remain thin. With the above considerations in mind, we proceed with analyses of a total of eight waveguides chosen from table 1.

3. Results and discussion

We analyze the graphene based waveguide resonators corresponding to the WR-6, WR-4, WR-3, WR-2.8, WR-2.2, WR-1.5, WR-1.2, and WR-1.0 waveguide sections listed in table 1. It is of interest to confirm the validity of the proposed concept throughout the frequency range from 100 GHz to 1100 GHz, and to check for the expected frequency dependence of the obtained tunability and loss. For each of the eight considered waveguides, resonator length is chosen so that the all-metal resonant frequency, $f_{\text{rez}}^{\text{M}}$, falls into the upper portion of the useful frequency range. Under the influence of the graphene surface impedance, the resonant frequency is shifted toward the lower end of the frequency range. To make different waveguide resonators comparable, the E -plane insert length is kept at a multiple of the waveguide broad wall a , in all analyzed cases. For the graphene-on-quartz resonators, where the complete length of an insert is covered by graphene, $l_{\text{T}} = 0.324a$ was considered. Similarly, in all simulations, the quartz thickness is a multiple of the waveguide broad wall, $d = a/16$. The results are summarized in table 2 and figure 5. The same eight values of the graphene chemical potential used in figure 3 were also utilized for the S -parameter calculation for each of the waveguide sections analyzed and presented in figure 5.

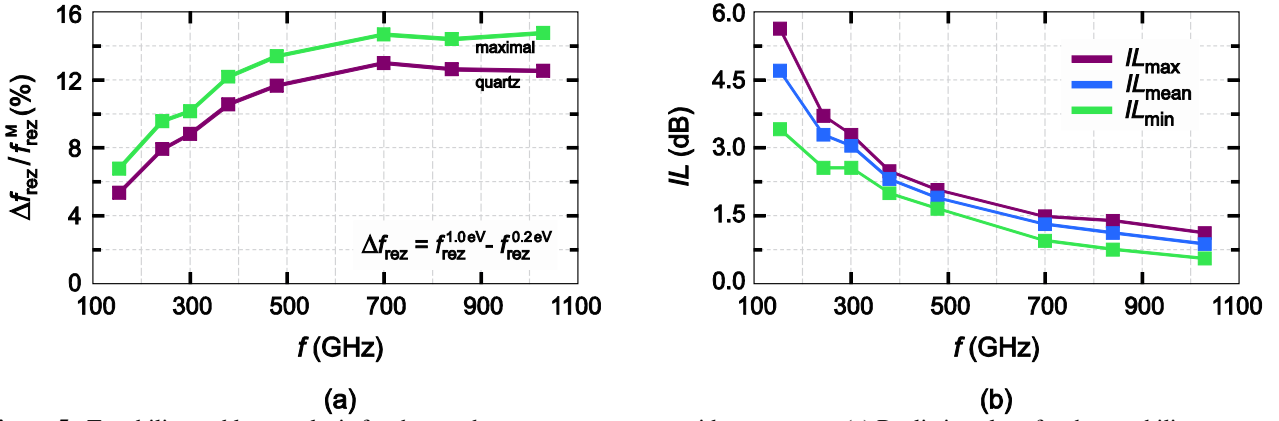


Figure 5. Tunability and loss analysis for the graphene-on-quartz waveguide resonators. (a) Realistic values for the tunability range ($R_g \neq 0$) are denoted as ‘quartz’. Theoretical maxima obtained assuming the lossless graphene are denoted as ‘maximal’ (for the chosen length of the E -plane inserts). (b) Insertion loss: mean value, maximum and minimum, for the graphene chemical potential varied in the range from 0.2 eV to 1.0 eV. Frequency points are determined by the f_{rez}^M for the considered waveguide section.

Results shown in figure 5 reveal the increase of the tunability range with frequency, with the obtained tunability percentage above 12% at higher frequencies, for the given insert length of $l_T = 0.324a$. Resonant frequencies for the all-metal resonators, for the two values of graphene chemical potential corresponding to the limits of the considered tunability range, as well as the resonant frequency for $\mu_c = 0.4$ eV, located close to the center of the tunability range, are listed in table 2. As it can be seen in figure 5, insertion loss decreases with frequency, which, along with the increase of tunability, makes the concept of graphene based waveguide resonators appealing for the considered frequency range. However, as it can be observed from figure 3(b), and this is similar for all considered frequencies, the loaded quality factor declines significantly for the lower values of the graphene chemical potential. The loaded quality factor is calculated as $Q_L = f_{\text{rez}} / BW_{3\text{dB}}$, with $BW_{3\text{dB}}$ denoting the 3 dB bandwidth of the S_{21} parameter. The graphene-on-quartz resonators are, in any case, characterized by the notably lower loaded quality factors than their pure metallic counterparts, and this is particularly pronounced for the lower chemical potential and larger impedances. Increase in the graphene surface impedance produces effects similar to the effects of varying the effective resonator length by changing the distance, l_{rez} , between the E -plane inserts. The same holds for the total length of the E -plane insert which appears effectively shorter and leads to the decline in the resonator quality factor. We address this issue by introducing the graphene-metal combined waveguide resonators. The graphene stripes are now located along the inner edges of the E -plane inserts, at the l_{rez} side, whereas the remaining parts of the inserts are covered by the Cu or Au thin film. Such configuration is expected to have less influence on the resonator quality factor; however, the decrease in tunability is also expected and has to be investigated.

Table 2. Graphene-on-quartz waveguide resonators: considered dimensions and resonant frequencies.

EIA / Ext.MIL	l_{rez} (μm)	l_T (μm)	f_{rez}^M (GHz)	$f_{\text{rez}}^{0.2\text{eV}}$ (GHz)	$f_{\text{rez}}^{0.4\text{eV}}$ (GHz)	$f_{\text{rez}}^{1.0\text{eV}}$ (GHz)
WR-6	720.0	535.3	155.00	143.00	147.50	151.25
WR-4	420.0	354.1	244.00	216.00	226.50	235.25
WR-3	360.0	280.0	300.75	262.00	276.00	288.50
WR-2.8	260.0	230.6	380.25	320.50	341.00	360.50
WR-2.2	210.0	181.2	479.50	393.75	421.25	449.50
WR-1.5	146.0	123.5	700.25	549.50	590.00	640.25
WR-1.2	132.0	98.8	840.50	656.00	700.00	762.00
WR-1.0	104.0	82.4	1029.50	786.50	835.00	915.50

The concept of the graphene-metal combined waveguide resonators is presented in figure 6, using the WR-2.2 waveguide section with the resonator length $l_{\text{rez}} = 210 \mu\text{m}$. The ratio l_T/a is varied as denoted in the figures. The S_{21} -parameter curves for the purely metallic resonators of the same sizes are denoted using the dash-dot-dot lines, with the resonant frequencies at about 480 GHz. In figure 6(a) we investigate the effect on the resonator parameters of the width of the graphene stripe, expressed as the percentage graphene with

respect to the E -plane insert length. To keep the graph less complicated, for each of the five compared graphene stripe widths, we only show the S_{21} -parameter for $\mu_c=0.4$ eV and $\mu_c=1.0$ eV. Each pair of lines corresponding to the same percent of graphene, p_g , is presented in distinctive color (shade of gray) in different line style. For better legibility, the data shown in figure 6(a) is also summarized in table 3.

As it can be concluded from figure 6(a) as well as the table 3, graphene percentage larger than 50% does not further improve the tunability; however, the quality factor decreases and the loss increases. Therefore, less than half of an insert could be covered by graphene. Please note, that the tunability range presented in table 3 differs from the one used throughout the paper due to the use of (0.4–1.0) eV range for the chemical potential. There already is a significant quality factor deterioration for $\mu_c=0.4$ eV, in comparison with the one for $\mu_c=1.0$ eV, with the increase in the graphene stripe width. This is even more pronounced for $\mu_c \in (0.2-1.0)$ eV, whereas the tunability is approximately doubled.

Table 3. Dependence of resonator properties on the width of graphene stripes (fixed total inserts length)^a.

$p_g = \frac{l_G}{l_T}$ (%)	Δf_{rez} (GHz) ^b	$T_p = \frac{\Delta f_{\text{rez}}}{f_{\text{rez}}^M}$ (%)	$IL^{0.4\text{eV}}$ (dB)	$IL^{1.0\text{eV}}$ (dB)	$Q_L^{0.4\text{eV}}$	$Q_L^{1.0\text{eV}}$
100.0	28.25	5.89	2.03	1.82	4.92	11.75
75.0	27.50	5.74	3.03	2.18	13.50	17.12
50.0	22.50	4.69	2.84	2.09	17.71	19.44
25.0	13.50	2.82	1.87	1.62	22.21	22.06
12.5	6.25	1.30	1.05	1.08	24.73	23.48

^a Data is obtained for the standard WR-2.2 waveguide section, with $l_{\text{rez}} = 210.0$ μm and $l_T = 181.2$ μm .

^b Chemical potential of graphene, μ_c , has been varied in the range (0.4–1.0) eV.

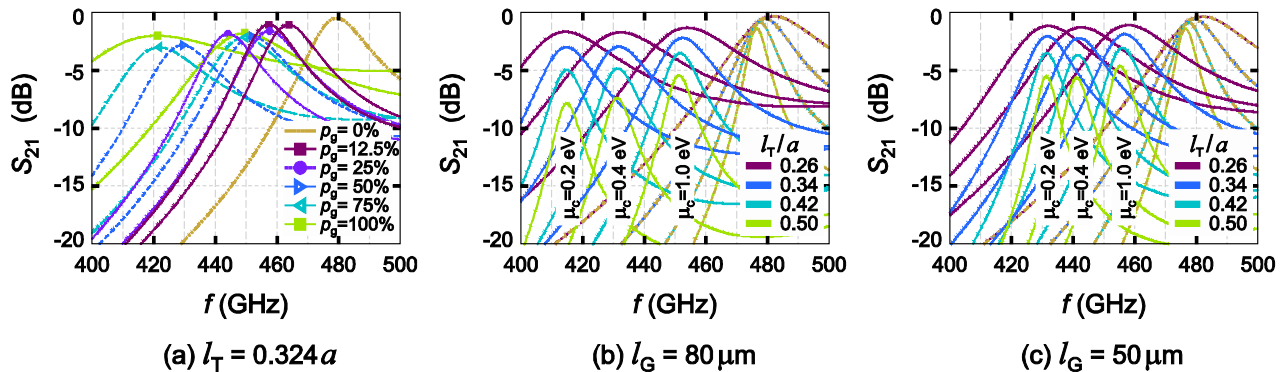


Figure 6. Graphene-metal combined waveguide resonators (WR-2.2 section). Graphene stripes are located along the inner edges of the E -plane inserts. (a) Effect of varying graphene stripe widths on tunability, insertion loss and quality factor of a resonator. Percentage of graphene larger than 50% of an insert does not notably improve tunability; however, it worsens the quality factor. (b) Effect of the E -plane insert length on quality factor and losses in graphene for the fixed width of the graphene stripe, $l_G = 80$ μm . (c) Effect of the E -plane insert length on quality factor and insertion loss for the fixed width $l_G = 50$ μm . Curves corresponding to the all-metal resonators are given by the golden dash-dot-dot lines ($f_{\text{rez}}^M \cong 480$ GHz).

As can be inferred from the above observations, the graphene-metal combined waveguide resonators can be carefully designed to meet the specific design requirements. Adjustment of the design parameters starts with the choice of the graphene stripe width, l_G , in accordance with the desired tunability range. This is illustrated by choosing $l_G = 80$ μm for the figure 6(b) and $l_G = 50$ μm for the figure 6(c). After that, the tunability remains almost the same for different total insert lengths, l_T . Optimizing a trade-off between the quality factor and the loss is the next step, in which the total E -plane insert length, l_T , is defined. With the increase of l_T , both the quality factor and the insertion loss increase. Relevant data for these two cases is summarized in table 4. We can conclude from the table 4 that obtained tunability percentages T_p (calculated very strictly, i.e., with respect to f_{rez}^M , which is always well above the device tunable bandwidth), in the considered examples range from around 5% to higher than 8%. Noting that wide tunability range is hard to obtain in submillimeter applications, and that even better tunability can be achieved using stripe widths wider than 80 μm , the reported tunability percentages are on the same order of magnitude as those in the state-of-the-art receivers [45], where several receivers are employed to cover wider submillimeter bandwidth.

Table 4. Dependence of resonator properties on the total length of an E -plane insert ^a.

E -plane insert length	Δf_{rez} (GHz) ^b	$T_p = \frac{\Delta f_{\text{rez}}}{f_{\text{rez}}^M}$ (%)	$IL^{0.2\text{eV}}$ (dB)	$IL^{1.0\text{eV}}$ (dB)	$Q_L^{0.2\text{eV}}$	$Q_L^{1.0\text{eV}}$	Q_L^M
Graphene stripe width $l_G = 80 \mu\text{m}$							
$l_T = 0.26 \cdot a$	39.75	8.29	1.71	1.34	11.68	12.62	15.56
$l_T = 0.34 \cdot a$	38.00	7.92	3.01	2.22	21.55	21.82	25.91
$l_T = 0.42 \cdot a$	36.75	7.66	5.01	3.55	34.58	34.75	42.44
$l_T = 0.50 \cdot a$	36.50	7.61	7.87	5.45	47.43	50.17	70.59
Graphene stripe width $l_G = 50 \mu\text{m}$							
$l_T = 0.26 \cdot a$	26.00	5.42	1.19	1.12	14.40	13.77	15.56
$l_T = 0.34 \cdot a$	25.00	5.21	2.09	1.91	26.17	24.04	25.91
$l_T = 0.42 \cdot a$	24.75	5.16	3.54	3.07	42.10	38.02	42.44
$l_T = 0.50 \cdot a$	23.75	4.95	5.55	4.64	63.93	55.18	70.59

^aData is obtained for the standard WR-2.2 waveguide section, with $l_{\text{rez}} = 210.0 \mu\text{m}$ and $a = 2b = 559.0 \mu\text{m}$.

^bChemical potential of graphene, μ_c , has been varied in the range (0.2–1.0) eV.

Reasons for the higher insertion loss of the graphene-metal combined waveguide resonators, in comparison with the initially analyzed graphene-on-quartz resonators, stem from the different boundary conditions at the E -plane inserts. Different boundary conditions mandate different EM field distribution in the vicinity of the inserts, as well as in the graphene stripe. Along the part of an E -plane insert covered by graphene, EM field complies with the equations (16a) and (16b), whereas in the metallic part of an insert the field vanishes. For a narrow graphene stripe and a longer metallic part of an insert, stronger field is generated. Simulation results for different graphene percentages, p_g , are presented in figure 7.

Dependence of the tunability, quality factor, and insertion loss on the graphene percentage, illustrated in figure 6(a), has been studied in detail taking the values from zero to $p_g = 100\%$, with the step of 2.5%, as an input parameter. The results are presented in figure 8. For the relatively narrow graphene stripes, with $p_g \leq 20\%$, the loaded quality factor remains close to the one corresponding to purely metallic inserts, $Q_L^M = 42.44$. At the same time, insertion loss is low and varies only slightly for the considered graphene chemical potential interval from 0.2 eV to 1.0 eV. Tunability of up to 5% can be achieved. These results agree with the third row describing the $l_G = 50 \mu\text{m}$ case in table 4, where $p_g = 21.3\%$. At about 50% graphene coverage of an insert, 10% tunability can be expected with the still very good quality factor of about 70% of Q_L^M . In this case loss is the highest. According to figure 8, the optimal width of the graphene stripe is from about 15% to approximately 40%, where the quality factor is high and consistent throughout the achieved tunability range.

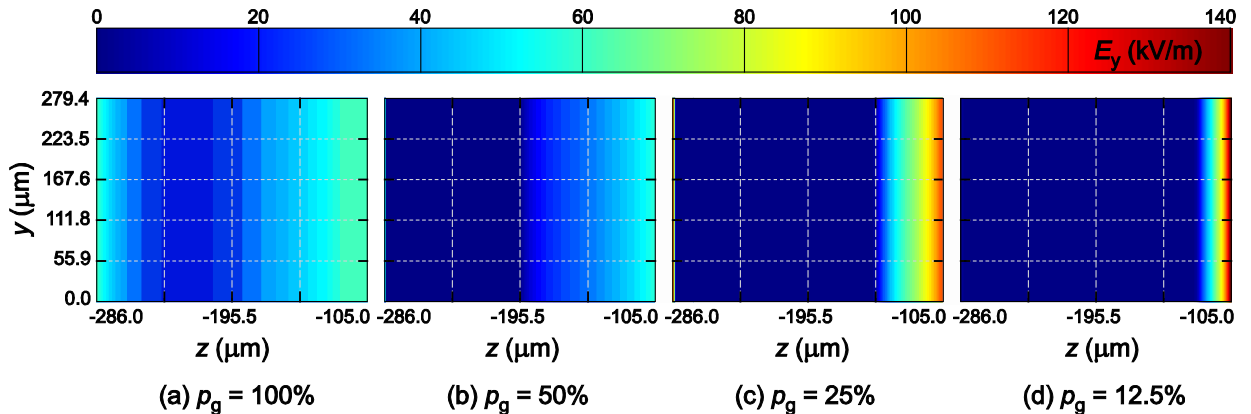


Figure 7. Electromagnetic field distribution along the E -plane insert for various widths of the graphene stripe. Graphene-metal combined waveguide resonators comply with the equations (16a), (16b), along the given percentage of an E -plane insert covered by graphene. In the metallic part of an insert, E_y approaches zero. Due to the differences of the structures considered in (a), (b), (c), and (d), and thus the field distributions, the relative impact of the variations in graphene surface impedance is larger for the smaller graphene percentage.

Frequency dependence of the key representative parameters of the graphene-metal combined waveguide resonators is given in figure 9. We again analyze the graphene based waveguide resonators corresponding to the WR-6, WR-4, WR-3, WR-2.8, WR-2.2, WR-1.5, WR-1.2, and WR-1.0 waveguides. Resonator length has been kept the same as in the previous analyses; it is listed in table 5, along with the chosen insert length, $l_T = 0.42a$. Quartz thickness is $d = a/16$, whereas the graphene stripe width is kept at 25% of an E -plane insert length in all the analyses. Resonant frequencies are listed in table 5, whereas the other results are shown in figure 9. There is a significant decrease of the insertion loss with frequency in the investigated frequency range. Quality factors at higher frequencies are excellent, represented in comparison with the Q_L^M . Tunability range in between 5% and 6% is obtained with the graphene-metal combined waveguide resonators, supporting the proposed concept as one of the possible solutions for the millimeter and submillimeter wave applications.

Table 5. Graphene-metal combined waveguide resonators: considered dimensions and resonant frequencies.

EIA / Ext.MIL	l_{rez} (μm)	l_T (μm)	f_{rez}^M (GHz)	$f_{\text{rez}}^{0.2\text{eV}}$ (GHz)	$f_{\text{rez}}^{0.4\text{eV}}$ (GHz)	$f_{\text{rez}}^{1.0\text{eV}}$ (GHz)
WR-6	720.0	693.4	154.75	144.50	148.25	151.25
WR-4	420.0	458.7	243.25	222.50	228.75	235.50
WR-3	360.0	362.7	299.75	273.00	280.50	289.25
WR-2.8	260.0	298.7	378.75	340.00	350.00	362.25
WR-2.2	210.0	234.7	477.50	426.00	438.00	454.25
WR-1.5	146.0	160.0	697.50	614.50	629.50	653.75
WR-1.2	132.0	128.0	838.50	742.50	758.00	784.00
WR-1.0	104.0	106.7	1028.25	900.50	917.50	949.50

5. Conclusion

A novel concept of tunable waveguide resonators for submillimeter wave applications has been studied in detail, following our promising preliminary investigation of WR-3 waveguide. Theoretical analysis has been presented, that could be used to develop customized software tools for the design of this type of waveguide resonators. Thorough full-wave numerical simulations covering several waveguide sections and frequencies ranging from 100 GHz to 1100 GHz confirmed the possibility of obtaining 5% tunability with excellently preserved resonator loaded quality factors, as well as larger tunability ranges, where the trade-off with quality factor and insertion loss is carried out. Tunable waveguide resonators are important basic building blocks of tunable filter devices, and the proposed concept is of great significance for the development of the compact and flexible components in the submillimeter wave spectral region.

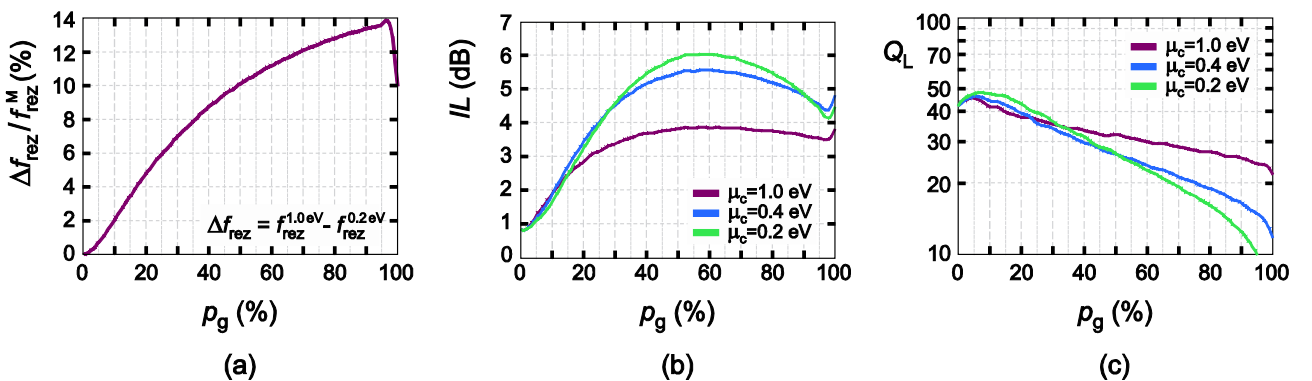


Figure 8. Detailed analysis of the dependence of (a) tunability range, (b) insertion loss, and (c) loaded quality factor, on the width of the graphene stripe expressed as the percentage of the E -plane insert length. WR-2.2 waveguide section with $l_{\text{rez}} = 210 \mu\text{m}$ and $l_T = 0.42a$ has been used for this analysis. Data is presented for the three values of graphene chemical potential, as denoted in the legend. The design of the graphene-metal combined waveguide resonators is subject to the trade-off between the tunability, quality factor, and loss. Optimal width of the graphene stripe is from 15% to about 40% of the E -plane insert length.

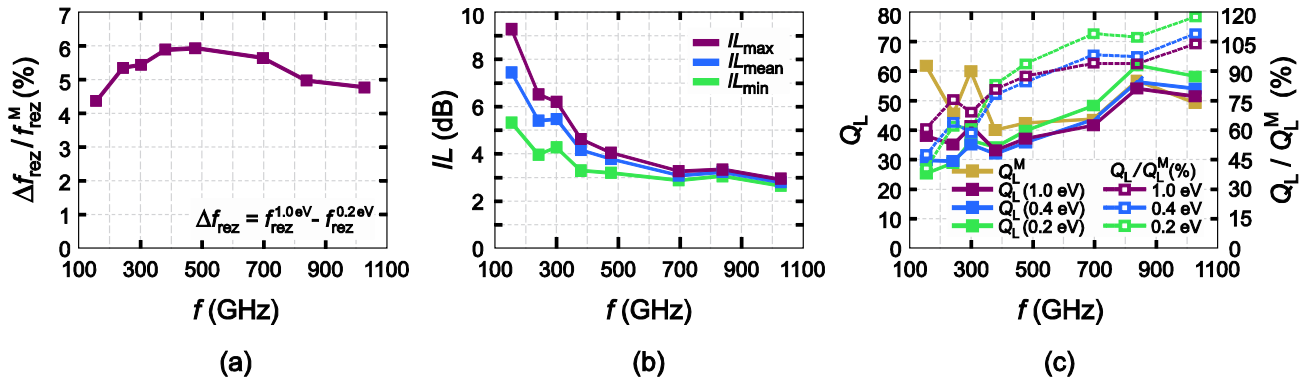


Figure 9. Comparative analysis of the (a) tunability range, (b) insertion loss, and (c) loaded quality factor, for the graphene-metal combined waveguide resonators covering the frequency range from 100 GHz to 1100 GHz. Frequency points correspond to the f_{rez}^M of the considered waveguide section. Reasonable tunability of 5% to 6% was obtained in all frequency intervals (a). Loss, calculated using the interval from 0.2 eV to 1.0 eV for μ_c , is somewhat higher than in the graphene-on-quartz case and should be compensated in the design (b). Absolute values of the loaded quality factor, including the pure metallic resonators of the given sizes, are shown in (c) by the filled squares and the solid lines. Quality factors of the combined resonators are shown as the percentage of Q_L^M , using the empty squares and the dashed lines.

Acknowledgments

This work was supported by the Serbian Ministry of Education, Science, and Technological Development under grant III-45003 and in part by the EU – Erasmus Mundus Action 2 project EUROWEB.

References

- [1] Zmuidzinas J and Richards P L 2004 Superconducting detectors and mixers for millimeter and submillimeter astrophysics *Proc. IEEE* **92** 1597–616
- [2] Appleby R and Anderton R N 2007 Millimeter-wave and submillimeter-wave imaging for security and surveillance *Proc. IEEE* **95** 1683–90
- [3] Globus T R, Woolard D L, Samuels A C, Gelmont B L, Hesler J, Crowe T W and Bykhovskaia M 2002 Submillimeter-wave Fourier transform spectroscopy of biological macromolecules *J. Appl. Phys.* **91** 6105–13
- [4] García-García J, Martín F, Miles R E, Steenson D P, Chamberlain J M, Fletcher J R and Thorpe J R 2002 Parametric analysis of micromachined reflex klystrons for operation at millimeter and submillimeter wavelengths *J. Appl. Phys.* **92** 6900–4
- [5] Song H-J and Nagatsuma T 2011 Present and future of terahertz communications *IEEE Trans. THz Sci. Technol.* **1** 256–63
- [6] Shang X, Ke M, Wang Y and Lancaster M J 2012 WR-3 band waveguides and filters fabricated using SU8 photoresist micromachining technology *IEEE Trans. THz Sci. Technol.* **2** 629–37
- [7] Chen Z, Zheng Y, Kang X, Lu B and Cui B 2013 WR-2.8 band micromachined rectangular waveguide filter *J. Infrared Millim. Terahertz Waves* **34** 847–55
- [8] Samoska L A 2011 An overview of solid-state integrated circuit amplifiers in the submillimeter-wave and THz regime *IEEE Trans. THz Sci. Technol.* **1** 9–24
- [9] Tamagnone M, Gomez-Diaz J S, Mosig J R and Perruisseau-Carrier J 2012 Reconfigurable terahertz plasmonic antenna concept using a graphene stack *Appl. Phys. Lett.* **101** 214102
- [10] Dragoman M, Muller A A, Dragoman D, Coccetti F and Plana R 2010 Terahertz antenna based on graphene *J. Appl. Phys.* **107** 104313
- [11] Mencarelli D, Bellucci S, Sindona A and Pierantoni L 2015 Spatial dispersion effects upon local excitation of extrinsic plasmons in a graphene micro-disk *J. Phys. D: Appl. Phys.* **48** 465104
- [12] Sensale-Rodriguez B, Yan R, Kelly M M, Fang T, Tahy K, Hwang W S, Jena D, Liu L and Xing H G 2012 Broadband graphene terahertz modulators enabled by intraband transitions *Nature Commun.* **3** 780
- [13] Li H-J, Wang L-L, Sun B, Huang Z-R and Zhai X 2014 Tunable mid-infrared plasmonic band-pass filter based on a single graphene sheet with cavities *J. Appl. Phys.* **116** 224505
- [14] Otsuji T, Boubanga Tombet S A, Satou A, Fukidome H, Suemitsu M, Sano E, Popov V, Ryzhii M and Ryzhii V 2012 Graphene-based devices in terahertz science and technology *J. Phys. D: Appl. Phys.* **45** 303001
- [15] Carrasco E, Tamagnone M and Perruisseau-Carrier J 2013 Tunable graphene reflective cells for THz reflectarrays and generalized law of reflection *Appl. Phys. Lett.* **102** 104103
- [16] Gomez-Diaz J S, Perruisseau-Carrier J, Sharma P and Ionescu A 2012 Non-contact characterization of graphene surface impedance at micro and millimeter waves *J. Appl. Phys.* **111** 114908
- [17] Hanson G W 2008 Dyadic Green's functions and guided surface waves for a surface conductivity model of graphene *J. Appl. Phys.* **103** 064302

- [18] Ilić A Ž and Budimir D 2014 Electromagnetic analysis of graphene based tunable waveguide resonators *Microw. Opt. Technol. Lett.* **56** 2385–8
- [19] Ridler N M and Ginley R A 2011 IEEE P1785: A new standard for waveguide above 110 GHz *Microwave Journal* **54** S20–4
- [20] Hesler J L, Kerr A R, Grammer W and Wollack E 2007 *Proc. 18th Int. Symposium on Space THz Technology (Pasadena, California, 21–23 March 2007)* ed A Karpov (Pasadena: Caltech) pp 100–3
- [21] Postoyalko V and Budimir D S 1994 Design of waveguide E-plane filters with all-metal inserts by equal ripple optimization *IEEE Trans. Microw. Theory Techn.* **42** 217–22
- [22] Kolundzija B and Djordjevic A 2002 *Electromagnetic Modeling of Composite Metallic and Dielectric Structures* (Norwood, MA: Artech House); WIPL-D 2013 WIPL-D Pro v11.0. Available: <http://www.wipl-d.com/>
- [23] ANSYS HFSS. Available: <http://www.ansys.com>
- [24] Collin R E 1991 *Field Theory of Guided Waves* (Piscataway, NJ: IEEE Press)
- [25] Konishi Y and Uenakada K 1974 The design of a bandpass filter with inductive strip – planar circuit mounted in waveguide *IEEE Trans. Microw. Theory Techn.* **22** 869–73
- [26] Arndt F, Bornemann J, Grauerholz D and Vahldieck R 1982 Theory and design of low-insertion loss fin-line filters *IEEE Trans. Microw. Theory Techn.* **30** 155–63
- [27] Lovat G 2012 Equivalent circuit for electromagnetic interaction and transmission through graphene sheets *IEEE Trans. Electromagn. Compat.* **54** 101–9
- [28] Svintsov D, Vyurkov V, Orlikovsky A, Ryzhii V and Otsuji T 2014 All-graphene field-effect transistor based on lateral tunnelling *J. Phys. D: Appl. Phys.* **47** 094002
- [29] Gomez-Diaz J S, Moldovan C, Capdevila S, Romeu J, Bernard L S, Magrez A, Ionescu A M and Perruisseau-Carrier J 2015 Self-biased reconfigurable graphene stacks for terahertz plasmonics *Nature Commun.* **6** 6334
- [30] Liu M, Yin X and Zhang X 2012 Double-layer graphene optical modulator *Nano Lett.* **12** 1482–5
- [31] Reina A, Jia X, Ho J, Nezich D, Son H, Bulovic V, Dresselhaus M S and Kong J 2009 Large area, few-layer graphene films on arbitrary substrates by chemical vapor deposition *Nano Lett.* **9** 30–5
- [32] Wei D, Mitchell J I, Tansarawiput C, Nam W, Qi M, Ye P D and Xu X 2013 Laser direct synthesis of graphene on quartz *Carbon* **53** 374–9
- [33] Vianco P T, Sifford C H and Romero J A 1997 Resistivity and adhesive strength of thin film metallizations on single crystal quartz *IEEE Trans. Ultrason, Ferroelect, Freq. Control* **44** 237–49
- [34] Lee S M and Krim J 2005 Scanning tunneling microscopy characterization of the surface morphology of copper films grown on mica and quartz *Thin Solid Films* **489** 325–9
- [35] Neugebauer P, Orlita M, Faugeras C, Barra A-L and Potemski M 2009 How perfect can graphene be? *Phys. Rev. Lett.* **103** 136403
- [36] Jablan M, Buljan H and Soljačić M 2009 Plasmonics in graphene at infra-red frequencies *Phys. Rev. B* **80** 245435
- [37] Bolotin K I, Sikes K J, Jiang Z, Klima M, Fudenberg G, Hone J, Kim P and Stormer H L 2008 Ultrahigh electron mobility in suspended graphene *Solid State Commun.* **146** 351–5
- [38] Bolotin K I, Sikes K J, Hone J, Stormer H L and Kim P 2008 Temperature-dependent transport in suspended graphene *Phys. Rev. Lett.* **101** 096802
- [39] Hirai H, Tsuchiya H, Kamakura Y, Mori N and Ogawa M 2014 Electron mobility calculation for graphene on substrates *J. Appl. Phys.* **116** 083703
- [40] Mayorov A S, Gorbachev R V, Morozov S V, Britnell L, Jalil R, Ponomarenko L A, Blake P, Novoselov K S, Watanabe K, Taniguchi T and Geim A K 2011 Micrometer-scale ballistic transport in encapsulated graphene at room temperature *Nano Lett.* **11** 2396–9
- [41] Varchon F, Feng R, Hass J, Li X, Ngoc Nguyen B, Naud C, Mallet P, Veuillen J-Y, Berger C, Conrad E H and Magaud L 2007 Electronic structure of epitaxial graphene layers on SiC: effect of the substrate *Phys. Rev. Lett.* **99**, 126805
- [42] Orlita M, Faugeras C, Plochocka P, Neugebauer P, Martinez G, Maude D K, Barra A-L, Sprinkle M, Berger C, de Heer W A and Potemski M 2008 Approaching the dirac point in high-mobility multilayer epitaxial graphene *Phys. Rev. Lett.* **101** 267601
- [43] Forti S and Starke U 2014 Epitaxial graphene on SiC: from carrier density engineering to quasi-free standing graphene by atomic intercalation *J. Phys. D: Appl. Phys.* **47** 094013
- [44] Ryzhii V, Dubinov A A, Otsuji T, Mitin V and Shur M S 2010 Terahertz lasers based on optically pumped multiple graphene structures with slot-line and dielectric waveguides *J. Appl. Phys.* **107** 054505
- [45] de Graauw Th *et al.* 2010 The Herschel-heterodyne instrument for the far-infrared (HIFI) *Astron. Astrophys.* **518** id. L6